Coaxial multishell nanowires with high-quality electronic interfaces and tunable optical cavities for ultrathin photovoltaics

Coaxial multishell nanowires with high-quality electronic interfaces and tunable optical cavities for ultrathin photovoltaics

Thomas J. Kempa[a,1], James F. Cahoon[a,1,2], Sun-Kyung Kim[a], Robert W. Day[a], David C. Bell[c], Hong-Gyu Park[b,3], and Charles M. Lieber[a,c,3]

[a]Department of Chemistry and Chemical Biology, Harvard University, Cambridge, Massachusetts 02138, [b]Department of Physics, Korea University, Seoul 136-701, Republic of Korea, [c]School of Engineering and Applied Sciences, Harvard University, Cambridge, Massachusetts 02138

Author Contributions: T.J.K., J.F.C., and C.M.L. designed research. T.J.K., J.F.C., S.-K.K., R.W.D., and D.C.B. performed experiments and analyses. S.-K.K. and H.-G.P. performed optical analyses through FDTD simulations. T.J.K., J.F.C., and C.M.L. wrote the paper.

The authors declare no conflict of interest.

[1]T.J.K and J.F.C. contributed equally to this work.

[2]Present address: Department of Chemistry, University of North Carolina at Chapel Hill, Chapel Hill, NC, 27599

[3]To whom correspondence should be addressed. E-mail: hgpark@korea.ac.kr (H.-G.P.); cml@cmliris.harvard.edu (C.M.L.)

This article contains supporting information.

Abstract. Silicon nanowires (NWs) could enable low-cost and efficient photovoltaics, though their performance has been limited by nonideal electrical characteristics and an inability to tune absorption properties. We overcome these limitations through controlled synthesis of a series of polymorphic core/multi-shell NWs with highly-crystalline hexagonally-faceted shells, and well-defined coaxial p-type/n-type (p/n) and p/intrinsic/n (p/i/n) diode junctions. Designed 200-300 nm diameter p/i/n NW diodes exhibit ultralow leakage currents of ~1 fA, and open-circuit voltages and fill-factors up to 0.5 V and 73%, respectively, under one-sun illumination. Single-NW wavelength-dependent photocurrent measurements reveal size-tunable optical resonances, external quantum efficiencies greater than unity, and current densities double those for silicon films of comparable thickness. In addition, finite-difference-time-domain simulations for the measured NW structures agree quantitatively with the photocurrent measurements, and demonstrate that the optical resonances are due to Fabry-Perot and whispering gallery cavity modes supported in the high-quality faceted nanostructures. Synthetically optimized NW devices achieve current densities of 17 mA/cm^2 and power conversion efficiencies of 6%. Horizontal integration of multiple NWs demonstrates linear scaling of the absolute photocurrent with number of NWs, as well as retention of the high open-circuit voltages and short-circuit current densities measured for single NW devices. Notably, assembly of 2 NW elements into vertical stacks yields short-circuit current densities of 25 mA/cm^2 with a back-side reflector, and simulations further show that such stacking represents an attractive approach for further enhancing performance with projected efficiencies of >15% for 1.2 μm thick 5 NW stacks.

Keywords: nanomaterials / solar cells / nanodevices / optical nanocavities/ nanophotonics

\body

Nanostructures and nanostructured materials may enable next-generation solar cells by providing for efficient charge separation (1-16) and tunable optical absorption (11, 17-19). Semiconductor nanowires (NWs) have exhibited promising efficiencies as single NW photovoltaic elements (8-11, 20-22) and as vertical arrays configured as photovoltaic (23-26) and photoelectrochemical (27, 28) solar cells, where the vertical array has been used to enhance light absorption (29). In the case of Si-based nanostructures, where Si photovoltaics represent benchmark systems with attractive material abundance and cost (30), the efficiency of NW devices has typically been limited by poor electrical performance and lack of tunable control of absorption properties at specific and broadband wavelengths. For example, previous reports of coaxial (8) and axially modulated (9) p-i-n single-NW photovoltaic devices yielded open-circuit voltages (V_{OC}) below 0.29 V, and, for coaxial devices, large leakage currents >1 pA. Furthermore, to accurately identify potentially unique absorption modes through photocurrent spectra and simulations, photonic devices must exhibit high-quality and reliable electrical characteristics, unlike previous devices (8). Vertical arrays of micron-diameter wires have shown better performance characteristics, yielding V_{OC} values of 0.50-0.56 V (19-21). However, preparation of microwire-based high V_{OC} photovoltaics (22) and photocathodes (29) has utilized high-temperature growth, dopant diffusion, and/or annealing processes (temperatures of 850 – 1000˚C), which limit precise structural control and involve high thermal cost. Here, we report bottom-up synthesis of a new class of core/multi-shell Si NWs that overcome the limitations typically encountered in nanoscale Si devices. *In situ* synthetic control of structural morphology, size, and doping provides a method to design rationally and tune the properties of these nanostructures. Furthermore, we establish the importance of strong optical resonances for controlling absorption

in the small, 200-300 nm diameter, NW cavities. This latter feature is distinct from the behavior in micro-wires and suggests NW structures as promising building blocks for new photonic and solar cell devices.

Results and Discussion

To probe key structural characteristics dictating the electronic and optical properties of these NWs, we designed, synthesized and characterized four distinct coaxial Si NW structures (Fig. 1A), in which doping in core and shell regions was varied *in situ*. We label these core/shell structures p/n, p/in, p/pn and p/pin according to the sequential doping of the core/shells, where p, i, and n refer to p-type, intrinsic and n-type, respectively, and the structures all share a common p-type Si NW core. Our synthetic protocol (see *Materials and Methods*) uses metal nanocluster-catalyzed, vapor-liquid-solid (VLS) growth for the p-Si NW core growth followed by vapor-solid (VS) growth of the shells. The thicknesses of the p, i and n-type shells were controlled precisely by growth time using independently characterized growth rates (see *Materials and Methods*). A representative field-emission scanning electron microscopy (SEM) image of a p/in coaxial Si NW (Fig. 1B) shows clear faceting with smooth facet surfaces distinct from the disordered and un-faceted nanocrystalline Si morphology reported previously (8). We note that clear faceting with smooth facet surfaces was achieved for each of the four types of coaxial structures (Fig. S1) and is indicative of highly crystalline shells in our NW structures.

To elucidate the crystalline structure of the core/shell NWs we have used high-resolution transmission electron microscopy (TEM) to image cross-sectional samples (see *Materials and Methods*). A representative bright-field image of a p/pin multi-shell structure (Fig. 1C) shows several key features. First, the shell of this p/pin structure consists of several distinct domains

ordered about the ~100 nm diameter NW core. Second, the electron diffraction pattern recorded from this sample yields clean, sharp spots characteristic of uniform diffraction from the [112] zone axis of the cubic Si crystal structure. These data show that the core and shell are coherently oriented in the <112> direction and thus indicate that the domains in the shell are separated by twist grain boundaries which preserve this direction. Third, lattice-resolved TEM images recorded near the outer region of the sample (Fig. 1D) show clear (111) lattice fringes up to the amorphous SiO_2 coating at the outermost edge of the NW. Also, on the basis of these images, surfaces of the NW can be assigned to two (111) planes, two (022) planes, and four (113) planes. Taken together, the TEM data and analysis suggest a unique, polymorphic shell structure composed of crystalline domains, which maintain coherent faceting and <112> crystal orientation along the length of the coaxial p/pin NW.

In addition, energy dispersive x-ray spectroscopy (EDS) was used to characterize the phosphorous dopant and oxygen profiles in a p/pin core/shell cross-sectional sample (Fig. 1E, and see *Materials and Methods*). The oxygen profile exhibits two peaks at the left and right edges of the sample arising from the SiO_2 layer on the faceted surfaces of the NW n-shell. The phosphorous profile also exhibits two peaks coincident with the left and right sides of the outer n-shell, which are shifted by 10-15 nm with respect to oxygen and have peak widths, 20-30 nm, in good agreement with the expected n-shell thickness of 25 nm based on measured growth rates. The relatively large apparent background signal in the phosphorous profile is an artifact resulting from mixed Si and P signals (Fig. S2). These measurements verify the capability to synthetically encode well-defined, nanoscale dopant variations in core/shell NWs and represent the first successful effort at mapping active dopants in complex NW structures. Together, these characterization results verify the synthesis of a new NW motif possessing precisely defined

nanometer-scale doped regions and a tunable crystal morphology.

Electrical transport properties of the four distinct classes of coaxial NWs were measured by fabrication of single NW devices with electrical contacts selectively defined to the p-type core and n-type shell (Fig. 2A, and see *Materials and Methods*). All current-voltage (*I*-V) characteristics (Fig. S3) were measured under air-mass 1.5 global (AM 1.5G) 1-sun (100 mW/cm^2) illumination, with current density (*J*) calculated using the projected NW area (8, 22, and see *Materials and Methods*). The illuminated *J*-V curves corresponding to each of the four distinct coaxial NW device structures (Fig. 2B) show progressive changes in V_{OC} and reveal several important features. First, the highest V_{OC} value, 0.48 V, is obtained for the p/in geometry and represents a substantial, two-fold improvement over our previous coaxial NWs with nanocrystalline shells (8), and is the highest V_{OC} reported to-date for a single Si NW device. We have attained V_{OC}'s > 0.47 V from devices with diameters as small as 200 nm, showing that much larger micron-scale diameters (22) are not necessary to achieve good performance. Second, the p/in device exhibits a fill factor (FF) of 73%, substantially higher than the 55% FF reported previously (8). The high FF combined with the steep slope of the *J*-V curve at V_{OC} are clear signatures of negligible series resistance in these devices. Third, for similar crystalline quality coaxial nanowires, the insertion of an ~30 nm intrinsic layer causes 140 mV (p/n to p/in) and 40 mV (p/pn to p/pin) improvements in V_{OC}. To further assess the control of junction properties in these core/multi-shell NWs, we examined the junction leakage current for the four distinct types of structures. A plot of V_{OC} versus the logarithm of the ratio of short-circuit current (I_{SC}) to dark saturation current (I_0) for sixteen total devices (Fig. 2C) is linear, as expected, with a monotonic increase in V_{OC} with decreasing I_0 (32, and see *Materials and Methods*). Significantly, the p/in device with V_{OC} = 0.48 V has a dark saturation current I_0 = 1.1 fA and current density J_0 = 0.34

fA/μm^2, which represents a 1000-fold improvement over our previous nanocrystalline-shell NW devices (8). The dramatic reduction in leakage current directly correlates with the two-fold improvement in V_{OC}. These data further support our conclusion that the synthetic control of NW structure has enabled improvements in all electronic metrics, V_{OC}, FF, I_0, relevant to photovoltaic devices.

Several groups have also postulated that metal nanocluster catalysts, especially gold, used to grow NWs could enhance recombination and adversely affect V_{OC} in NW devices (33). Although our V_{OC} values for Au-nanocluster catalyzed NWs already suggest a level of material quality approaching that of good planar Si devices (see *Materials and Methods*), we have further investigated this point. First, NWs were synthesized using Al (Fig. S4) as the metal catalyst (33) because Al, unlike Au, does not act as a mid-band gap trap state in Si (34). Notably, the best illuminated *I*-V curve for an p/pin diode geometry (Fig. 2D, grey curve) yields a V_{OC}, 0.23 V, ~2 times smaller than the value for analogous Au-catalyzed devices. Second, removal of Au catalysts from as-grown NW cores (see *Materials and Methods*) to preclude incorporation of Au during the higher temperature shell growth steps (Fig 2D, red curve) yielded a device with V_{OC}, 0.44 V, similar to our best results for coaxial NWs prepared without removal of the catalyst. Together, these results show that proposed Au impurities do not adversely lower V_{OC}, and suggest that the overall quality of the core/multi-shell structure is more important for our NW devices. In addition, measurements made before and after passivation of the outermost n-shell (black curves, Fig. 2D) show that surface oxidation yields an ~58 mV increase in V_{OC}, suggesting that surface recombination has only a small effect on the overall V_{OC} of our best coaxial NW devices. In summary, comparisons among the four classes of polymorphic core/multi-shell NWs as well as with previous core/nanocrystalline-shell NWs (8) demonstrate

that our *in situ* synthetic control enables realization of optimized p/in and p/pin NW structures with high electrical performance as manifest by the substantially improved V_{OC}, FF and I_O values.

The p/in and p/pin core/multi-shell NW devices (Fig. 2B) also exhibit J_{SC} values, 8-10 mA/cm^2, substantially larger than expected for an equivalent thickness of bulk Si (32). Data obtained on NW devices with lengths spanning over 1 order of magnitude (Fig. S5) exhibit linear scaling of I_{SC} and nearly constant J_{SC}, suggesting that the high J_{SC} values are intrinsic to these nanoscale structures and are not due to extrinsic factors such as scattering by contact electrodes (8). To understand the origin of these large J_{SC} values, we carried out wavelength-dependent photocurrent measurements and finite-difference time-domain (FDTD) simulations on individually-characterized core/multi-shell NW devices (see *Materials and Methods*). A representative curve of the absolute external quantum efficiency (EQE) versus wavelength acquired for a p/in NW device (Fig. 3A, black curve; Fig. S6) and the corresponding simulated EQE spectrum (Fig. 3A, red dashed curve) demonstrate several important points. First, the experimental and simulated spectra are highly structured, with very good agreement in the peak positions. Significantly, from analysis of the simulations and polarization-dependent experiments (Fig. S6) we can assign peaks in EQE to wavelength-dependent Fabry-Perot (Fig. 3 labels 1, 2, 4, and 5) and whispering-gallery (Fig. 3 labels 3 and 6) resonant absorption modes within the hexagonal NW structure. Second, there is excellent correspondence in absolute EQE amplitudes between experiment and simulation, where the full-field FDTD simulations are executed without adjustable parameters and assume that internal quantum efficiency (IQE) has value of unity (see *Materials and Methods*). This agreement in amplitudes further supports the use of NW projected area in calculation of current densities, and moreover, indicates that charge recombination is

minimized in our new p/in and p/pin core/multi-shell structures. Third, the EQE spectrum approaches and even exceeds unity for wavelengths in the range of 400-500 nm. EQE values greater than unity are possible because of an optical antenna effect (17, 18), in which the absorption cross-section of the NW exceeds its physical cross-section for some photon energies. This phenomenon is a purely classical effect caused by the sub-wavelength diameter of the NW and is quantitatively reproduced by the FDTD simulations.

To illustrate how rational synthetic design can be used to tune absorption within our NW photovoltaic elements, we examined a larger diameter (305 vs. 240 nm) p/pin NW device. The measured and simulated absolute EQE spectra for the p/pin device (Fig. 3B, Fig. S6C) exhibit several features differentiating them from the corresponding spectra discussed above for the p/in NW device. First, peaks 4 – 6 in the p/pin spectrum (Fig. 3B), which correspond to the same modes (Fig. 3C) represented by peaks 1 – 3 in the p/in spectrum (Fig. 3A), are substantially red-shifted. Second, the p/pin device exhibits a larger number of peaks in the experimental and simulated EQE spectra. Third, the p/pin experimental spectrum (Fig. 3B) exhibits two peaks between 470 and 520 nm with near-unity amplitudes. These two peaks correspond to resonant modes localized near the core-shell interface (Fig. 3C: label 4). We suggest that the higher than predicted EQE values may result from enhanced absorption within the first ~20 nm of the polymorphic p-shell surrounding the p-core, although future studies will be needed to confirm and potentially exploit these differences in detail. The observed red-shifted modes with enhanced absorption are also better matched in frequency to the maximum irradiance of the solar spectrum (Fig. 3B, blue dashed curve). This observation explains the ~40% larger J_{SC} of p/pin NWs compared to p/in NWs (Fig. 2B), and underscores our ability to optimize device performance through synthetic tuning of nanostructures.

We also compared the experimental and simulated optical properties of a p/in core/multi-shell NW (Fig. 3A) to an equivalent thickness of bulk Si. The simulated EQE spectrum for 240 nm of bulk Si (Fig. 3A, dashed green line) is featureless and shows substantially lower amplitude than the p/in NW. The origin of the differences in EQE spectra can be understood by comparing the interaction of light with both structures. For example, a plot of the electrical field intensity for an incident plane wave with a wavelength of 445 nm (Fig. 3D) shows a strong resonant mode excited within the NW, but the profile of electric field within an equivalent thickness of bulk Si is featureless. These modes in the NWs lead to substantial and structured J_{SC} contribution from the shell through much of the core, while bulk Si exhibits the standard exponential decay as function of thickness (Fig. 3D). Significantly, the spatial localization and intensity of resonant modes could be adjusted by tuning the morphology of the NW cavity.

The studies discussed above demonstrate substantial improvement in the photovoltaic properties of Si NWs at the single NW level. To determine whether J_{SC} could be improved further, we fabricated NW devices on transparent quartz substrates and measured *J*-V characteristics with and without a silver metal back-side reflector (BSR), as shown in Figure 4A. Without the BSR, a representative single p/pin device (red line) yields J_{SC} = 9.8 mA/cm^2 and an overall conversion efficiency, η, of 3.2%. Significantly, the same device with a BSR yields J_{SC} = 17.0 mA/cm^2 and η = 5.9%. The substantial increase in efficiency achieved with the BSR thus suggests one straightforward route to mitigate incomplete absorption and thereby enable efficient nanowire-based solar cells.

While individual NW photovoltaics represent the ideal platform for elucidating fundamental factors affecting device efficiency and can be used to power nanoelectronic elements (8), it is also important to consider the prospects for scaling these to arrays that will be

required for solar cells. As an initial step in this direction we interconnected in parallel from 1 to 8 p/pin core/multi-shell NW elements. Measurements of light *I*-V data from these small multi-NW devices (inset, Fig. 4B) show good 'cell' characteristics are maintained (e.g., V_{OC} and FF are nearly constant) with increasing number of NW elements. Indeed, the FF for the 8 NW device , 69.3%, is similar to the best value we achieved on single NW elements, 68.0%. Moreover, and central to the potential for scaling, we observe a step-wise increase in I_{SC} from 191 to 1723 pA as the number of NWs in a device is increased from 1 to 8, respectively (Fig. 4B). Importantly, this increase in absolute I_{SC} is also accompanied by preservation of J_{SC} to within 3% of that for the best single NW device. We believe these results show that assembly and large-scale integration could be a viable strategy for using our core/multi-shell nanowire building blocks, although future studies will be required to expand to larger arrays. Such work should be able to exploit reported advances in assembly of dense parallel nanowires on the micrometer to several inch scale (35), where the nanowires have also exhibited good electronic properties (35, 36).

Furthermore, we propose and describe here a new paradigm for significantly enhancing current density and thereby efficiency, which involves layering and interconnecting designed coaxial core/multi-shell NW components. To demonstrate this new concept we have assembled vertical stacks of horizontally-oriented NW devices (see *Materials and Methods*). A representative SEM image of the assembled NWs (inset, Fig. 5A) shows the well-aligned vertical stack of two p/pin NWs on a quartz substrate. Transport measurements for the vertical stack of two parallel connected p/pin NWs yield a J_{SC} of 14.0 mA/cm^2 (Fig. 5B), which represents a 1.4x increase compared to the best single p/pin NW device. Significantly, the experimental EQE spectrum for the stacked double NW device (Fig. 5A) shows that nearly all peaks from 380 – 700 nm coincide in frequency with those for a single NW device, and that the EQE amplitudes are

increased by a factor of 1.0 – 2.0 across this wavelength range. These increased amplitudes account for the observed 40% J_{SC} enhancement, and notably, FDTD simulations reproduce the EQE enhancement for the double stack configuration and predict a comparable 41% increase in J_{SC}. Simulations also show that the resonant modes present in a single or in this case the top NW are preserved in the bottom NW, and this effect permits the broadband enhancement observed in the experimental and simulated EQE spectra for the double-NW stack (Fig. S7). In addition, we explored the scaling of our new concept by simulating NW stack structures with up to five equal diameter NWs and a total thickness of 1.2 μm (Fig. 5B and Fig. S7). Comparison of the J_{SC} and EQE for the 5-NW stack and a single microwire with a diameter of the same height shows that the 5-NW stack is predicted to have 26% higher J_{SC} and 2-fold higher EQE at 620 nm, with the EQE of the stack exceeding that of the microwire for most wavelengths (Fig. S7B). Notably, simulations show that a stack of five NWs could yield J_{SC} values of 24 and >40 mA/cm^2 without and with a BSR, respectively, values that could yield power-conversion efficiencies >15%.

Conclusions

Designed 200-300 nm polymorphic core/multi-shell NWs exhibit excellent photovoltaic properties including high open-circuit voltages up to 0.5 V, ultra-low leakage currents of < 1 fA, and optimized short circuit current densities of over 10 mA/cm^2. Large and wavelength tunable nanowire resonant cavity modes lead to light absorption substantially greater than in equivalent thickness thin films, and yield EQE values above unity for specific modes. Optimized devices yield J_{SC} = 17 mA/cm^2 and an efficiency of 6%. Integration of multiple devices in parallel demonstrates linear scaling of photocurrent and excellent preservation of device properties,

including the high V_{OC}, J_{SC}, and FF values observed in single NW devices. In addition, we have introduced a new paradigm for 'building' ultrathin photovoltaics through the stacking of designed NW elements, and show that approximately 1 μm thick vertical stacks consisting of 5 NWs could yield efficiencies in excess of 15%. While future studies will be needed to develop further these concepts, we believe that our results demonstrate substantial promise for single and multi-layer interconnected assemblies of these core/multi-shell NW building blocks, including structures tailored to enhance absorption in different regions of the solar spectrum, for the development of next-generation, ultrathin solar cells.

Materials and Methods

The materials and methods can be found in the supporting information for this paper.

Acknowledgments

We thank B. Tian and J. Huang for helpful discussions. C.M.L. acknowledges support from a National Security Science and Engineering Faculty Fellow (NSSEFF) award. H.-G.P. acknowledges support of this work by Creative Research Initiatives (2011-0000419) of MEST/KOSEF. J.F.C. acknowledges an Intelligence Community Postdoctoral Research Fellowship. T.J.K. and R.W.D. acknowledge NSF Graduate Research Fellowships.

References

1. Blankenship RE *et al.* (2011) Comparing photosynthetic and photovoltaic efficiencies and recognizing the potential for improvement. *Science* 332:805-809.

2. Hochbaum AI, Yang PD (2010) Semiconductor nanowires for energy conversion. *Chem. Rev.* 110:527-546.

3. Zhu J, Yu Z, Fan S, Cui Y (2010) Nanostructured photon management for high performance solar cells. *Mater. Sci. Eng. R* 70:330-340.

4. Zhu J, Hsu CM, Yu, Z, Fan S, Cui Y (2009) Nanodome solar cells with efficient light management and self-cleaning. *Nano Lett.* 9:1979-1984.

5. Wang XD, Song JH, Liu J, Wang ZL (2007) Direct-current nanogenerator driven by ultrasonic waves. *Science* 316:102-105.

6. Tang J, Huo Z, Brittman S, Gao H, Yang PD (2011) Solution-processed core-shell nanowires for efficient photovoltaic cells. *Nature Nanotechnol.* 6:568-572.

7. Peng KQ, Lee ST (2011) Silicon nanowires for photovoltaic solar energy conversion. *Adv. Mater.* 23:198-215.

8. Tian BZ *et al.* (2007) Coaxial silicon nanowires as solar cells and nanoelectronic power sources. *Nature* 449:885-889.

9. Kempa TJ *et al.* (2008) Single and tandem axial p-i-n nanowire photovoltaic devices. *Nano Lett.* 8:3456-3460.

10. Tian B, Kempa TJ, Lieber CM (2009) Single nanowire photovoltaics. *Chem. Soc. Rev.* 38:16-24.

11. Dong Y, Tian B, Kempa TJ, Lieber CM (2009) Coaxial group III-nitride nanowire photovoltaics. *Nano Lett.* 9:2183-2187.

12. Kayes BM, Atwater HA, Lewis NS (2005) Comparison of the device physics principles of planar and radial p-n junction nanorod solar cells. *J. Appl. Phys.* 97:114302-114311.

13. Gur I, Fromer NA, Chen CP, Kanaras AG, Alivisatos AP (2007) Hybrid solar cells with prescribed nanoscale morphologies based on hyperbranched semiconductor nanocrystals. *Nano Lett.* 7:409-414.

14. Fan ZY *et al.* (2009) Three dimensional nanopillar array photovoltaics on low cost and flexible substrates. *Nature Mater.* 8:648-653.

15. Chang, JA *et al.* (2010) High-performance nanostructured inorganic-organic heterojunction solar cells. *Nano Lett.* 10:2609-2612.

16. Luther, JM *et al.* (2007) Multiple exciton generation in films of electronically coupled PbSe quantum dots. *Nano Lett.* 7:1779-1784.

17. Cao, L *et al.* (2009) Engineering light absorption in semiconductor nanowire devices. *Nature Mater.* 8:643-647.

18. Cao, LY *et al.* (2010) Semiconductor nanowire optical antenna solar absorbers. *Nano Lett.* 10:439-445.

19. Kamat PV (2008) Quantum dot solar cells. Semiconductor nanocrystals as light harvesters. *J. Phys. Chem. C* 112:18737-18753.

20. Colombo C, Heibeta M, Gratzel M, Fontcuberta i Morral A (2009) Gallium arsenide p-i-n radial structures for photovoltaic applications. *Appl. Phys. Lett.* 94:173103-173108.

21. Heurlin M *et al.* (2011) Axial InP nanowire tandem junction grown on a silicon substrate. *Nano Lett.*, 11:2028-2031.

22. Kelzenberg MD *et al.* (2011) High-performance Si microwire photovoltaics. *Energy Environ. Sci.* 4:866-871.

23. Putnam MC *et al.* (2010) Si microwire-array solar cells. *Energy Environ. Sci.* 3:1037-1041.

24. Kendrick CE *et al.* (2010) Radial junction silicon wire array solar cells fabricated by gold-catalyzed vapor-liquid-solid growth. *Appl. Phys. Lett.* 97:143108.

25. Yoon HP *et al.* (2010) Enhanced conversion efficiencies for pillar array solar cells fabricated from crystalline silicon with short minority carrier diffusion lengths. *Appl. Phys. Lett.* 96:213503.

26. Garnett E, Yang PD (2010) Light trapping in silicon nanowire solar cells. *Nano Lett.* 10:1082-1087.

27. Law M, Greene LE, Johnson JC, Saykally R, Yang P (2005) Nanowire dye-sensitized solar cells. *Nature Mater.* 4:455-459.

28. Boettcher SW *et al.* (2010) Energy-conversion properties of vapor-liquid-solid-grown silicon wire-array photocathodes. *Science* 327:185-187.

29. Kelzenberg MD *et al.* (2010) Enhanced absorption and carrier collection in Si wire arrays for photovoltaic applications. *Nature Mater.* 9:239-244.

30. Wadia C, Alivisatos AP, Kammen DM (2009) Materials availability expands the opportunity for large-scale photovoltaics deployment. *Environ. Sci. Technol.* 43:2072-2077.

31. Green MA, Emery K, Hishikawa Y, Warta W (2010) Solar cell efficiency tables (version 36). *Prog. Photovoltaics* 18:346-352.

32. Jeffery LG (2004) in *Handbook of Photovoltaic Science and Engineering,* ed Hegedus S, Luque A (Wiley, New York), pp 61-112.

33. Ke Y *et al.* (2009) Fabrication and electrical properties of Si nanowires synthesized by Al catalyzed vapor-liquid-solid growth. *Nano Lett.* 9:4494-4499.

34. Schmidt V, Wittemann JV, Gosele U (2010) Growth, thermodynamics, and electrical properties of silicon nanowires. *Chem. Rev.* 110:361-388.

35. Fan ZY *et al.* (2008) Wafer-scale assembly of highly ordered semiconductor nanowire arrays by contact printing. *Nano Lett.* 8:20-25.

36. Javey A, Nam SW, Friedman RS, Yan H, Lieber CM (2007) Layer-by-layer assembly of nanowires for three-dimensional, multifunctional electronics. *Nano Lett.* 7:773-777.

Figure Legends

Fig. 1. Design, synthesis, and characterization of polymorphic core/multi-shell NWs. *(A)* Three dimensional schematic of a typical core/shell NW and cross-sectional schematics of four core/shell diode geometries investigated as standalone single NW solar cells. *(B)* SEM image of an as-grown, core/shell p/in Si NW; scale bar, 100 nm. *(C)* Left: bright-field TEM image of a NW cross-section showing a core surrounded by crystalline shell; scale bar, 50 nm. Right: electron diffraction pattern for the cross section on left showing it is oriented along the [112] zone axis. *(D)* High resolution bright-field, aberration-corrected TEM image at the (022), (113) vertex of a NW cross section revealing clear lattice fringes; scale bar, 5 nm. *(E)* Phosphorous (red) and oxygen (green) line profiles across a NW cross-section acquired from EDS elemental mapping on an aberration-corrected STEM. Inset: cs-STEM image of NW cross-section from which data was taken; scale bar, 100 nm.

Fig. 2. Transport properties of single NW solar cells. *(A)* SEM image of a standalone NW device with lithographically defined Ti/Pd contacts overlapping the shell and core regions of the NW; scale bar, 1 μm. Inset: SEM image of a single core/shell NW transferred onto a Si_3N_4 substrate and wet-chemically etched on the lower portion to reveal the core; scale bar, 200 nm. *(B)* Current density-voltage (*J*-V) characteristics of single NW solar cells composed of four distinct diode geometries (refer to Fig. 1A). *(C)* Open-circuit voltage (V_{OC}) versus the logarithm of the ratio of short-circuit current (I_{SC}) to dark saturation current (I_0) for the four best devices from each diode geometry. A fit (dashed line) to the ideal diode equation yields an ideality factor n = 1.28. This value is lower than those calculated from dark *I*-V data for individual devices, although we note that our values for n (1.3 – 1.8) indicate consistently the presence of carrier recombination within the depletion region of all devices. *(D)* Current-voltage characteristic (red)

for a p/in NW device for which Au catalyst was removed by aqueous KI/I_2 wet-chemical etch prior to shell growth. Grey curve is for an i/pin Si NW device whose growth was catalyzed by Al. Black curves show current-voltage characteristics for a single Au-catalyzed p/in NW device measured before and after oxidation of its surface in air for one week.

Fig. 3. Enhanced and tunable absorption in NWs. *(A)* External quantum efficiency (EQE) as a function of wavelength for a p/in NW (black curve) and simulated EQE spectrum (dashed red curve) produced with no adjustable parameter other than the size of the NW (height of 240 nm). Dashed green curve shows the simulated spectrum for top 240 nm of planar bulk Si. *(B)* EQE spectrum (black curve) of a p/pin NW compared to the irradiance of the AM1.5G solar spectrum (dashed blue curve). Dashed red curve corresponds to simulated EQE calculated with no other adjustable parameter besides the NW size (height of 305 nm). *(C)* FDTD simulations of resonant mode spatial profiles for p/in (profiles 1-3) and p/pin (profiles 4-6) structures. Labeled profiles correspond to the EQE peaks labeled identically within Fig. 3A-B and profiles in each column correspond to the same mode excited within both structures. All profiles are for TM polarizations and use a linear color scale representing absorption (not electric field intensity) within the mesoscopic structures. Resonant modes labeled 3 and 6 correspond to whispering-gallery type modes while all others correspond to Fabry-Perot resonances. *(D)* Plot of electric field intensity for plane wave (λ = 445nm) interacting with a NW (left) and bulk Si (right). White line defines outline of NW and top surface of bulk Si. Beneath are plots of total J_{SC} as a function of position inside the NW or bulk Si.

Fig. 4. Integration of NW components for efficient solar cells. *(A)* Current density-voltage (*J*-V) characteristics for a p/pin device without (red curve) and with a Ag back-side reflector (purple curve) under 1-sun illumination. Inset: schematic of the device layout on quartz. *(B)*

Linear scaling of I_{SC} (black squares and shaded blue bars) and preservation of J_{SC} (orange circles and line) as multiple p/pin NWs are integrated in parallel. Inset: light *I-V* curves for devices consisting of 1-8 NWs connected in parallel.

Fig. 5. Vertical assembly of layered NW components for efficient solar cells. *(A)* Experimental EQE spectrum for double-NW vertical stack (thick black line) and for single NW (thin black line) device. Both devices are on quartz without back-reflectors. Simulated EQE spectrum for the double-NW stack (dashed red line) using NWs with a Si height of 250 nm. Inset: SEM of a device consisting of two NWs stacked on quartz substrate and electrically connected in parallel; scale bar, 500 nm. *(B)* Experimental current densities for a single NW device (diamonds) and stacked double NW device (squares) under AM 1.5G 1-sun illumination. Red markers show data without a Ag-metal BSR and purple markers data with the Ag-metal BSR. Dashed red and purple curves denote simulated current densities for stacked NWs with increasing number of NWs in the stack (N = 1, 2, 3, 4, 5) without and with a BSR, respectively.

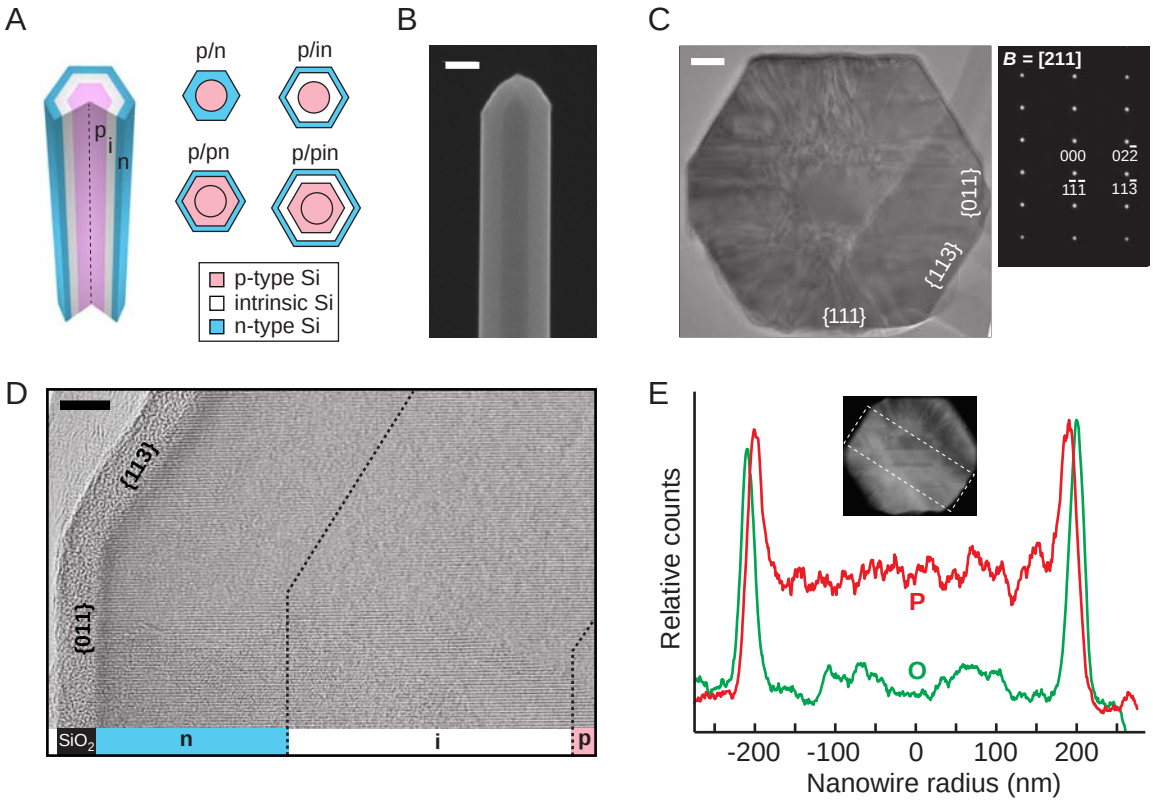
A
p/n
p/in
p/pn
p/pin
p
i
n
p-type Si
intrinsic Si
n-type Si
B
C
B = [211]
000
022
111
113
{011}
{113}
{111}
D
{113}
{011}
SiO2
n
i
p
E
Relative counts
P
O
-200
-100
0
100
200
Nanowire radius (nm)

Figure 1

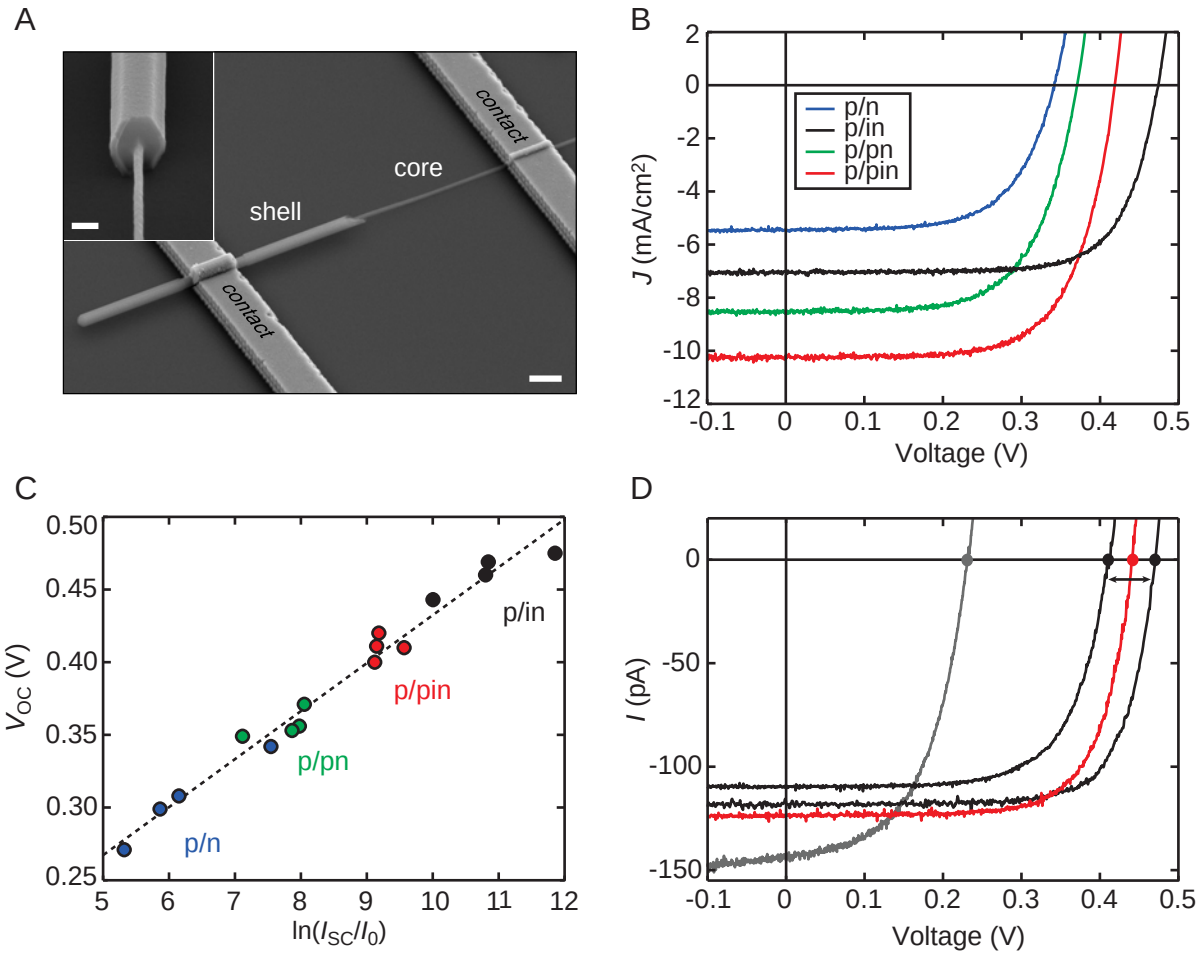
A
contact
core
shell
contact
B
p/n
p/in
p/pn
p/pin
J (mA/cm²)
Voltage (V)
C
p/in
p/pin
p/pn
p/n
V_OC (V)
ln(I_SC/I_0)
D
I (pA)
Voltage (V)

Figure 2

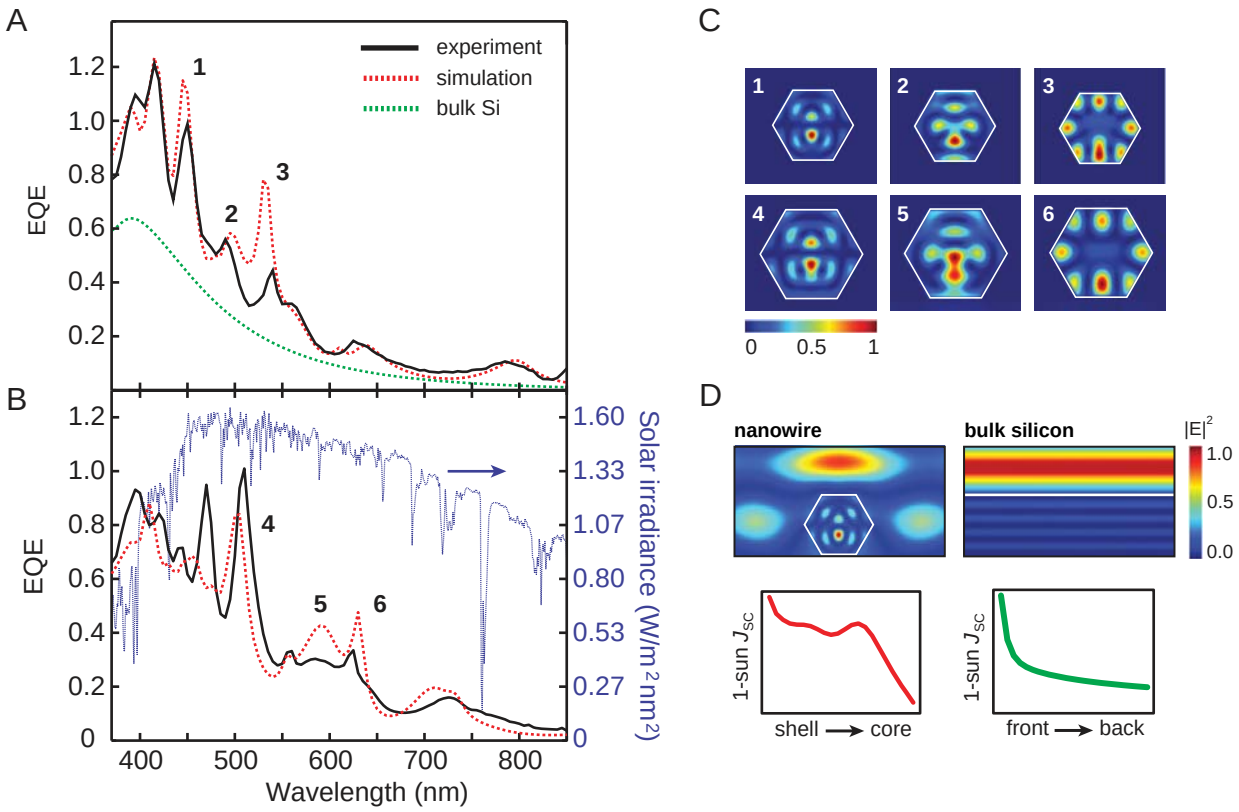
A
B
C
D
experiment
simulation
bulk Si
EQE
Wavelength (nm)
Solar irradiance (W/m² nm²)
nanowire
bulk silicon
|E|²
1-sun J_SC
shell → core
front → back

Figure 3

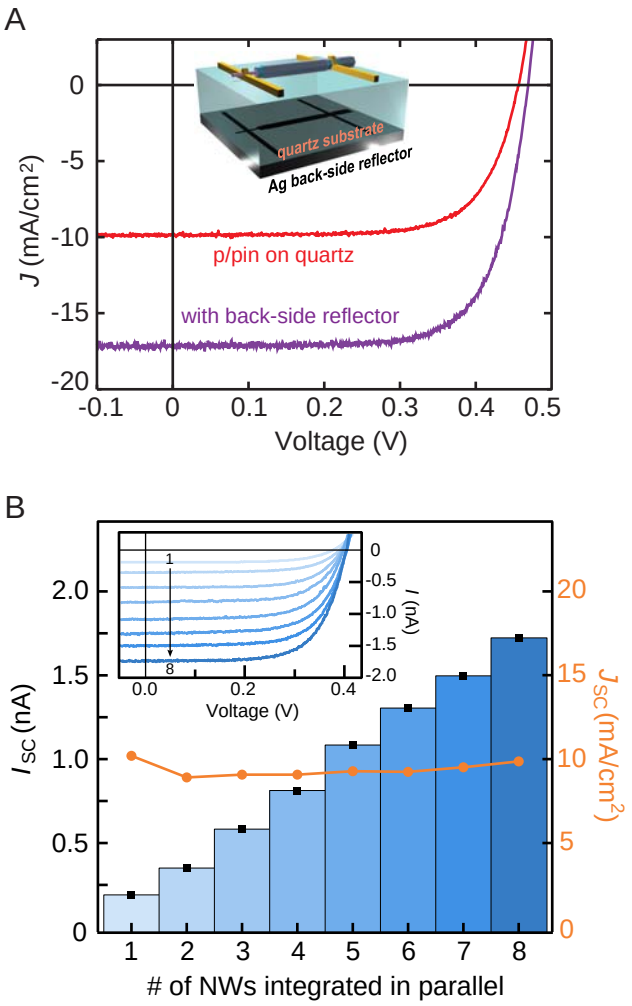
A
0
-5
-10
-15
-20
J (mA/cm²)
-0.1
0
0.1
0.2
0.3
0.4
0.5
Voltage (V)
quartz substrate
Ag back-side reflector
p/pin on quartz
with back-side reflector
B
2.0
1.5
1.0
0.5
0
I_SC (nA)
20
15
10
5
0
J_SC (mA/cm²)
1
2
3
4
5
6
7
8
# of NWs integrated in parallel
1
8
0.0
0.2
0.4
Voltage (V)
0
-0.5
-1.0
-1.5
-2.0
I (nA)

Figure 4

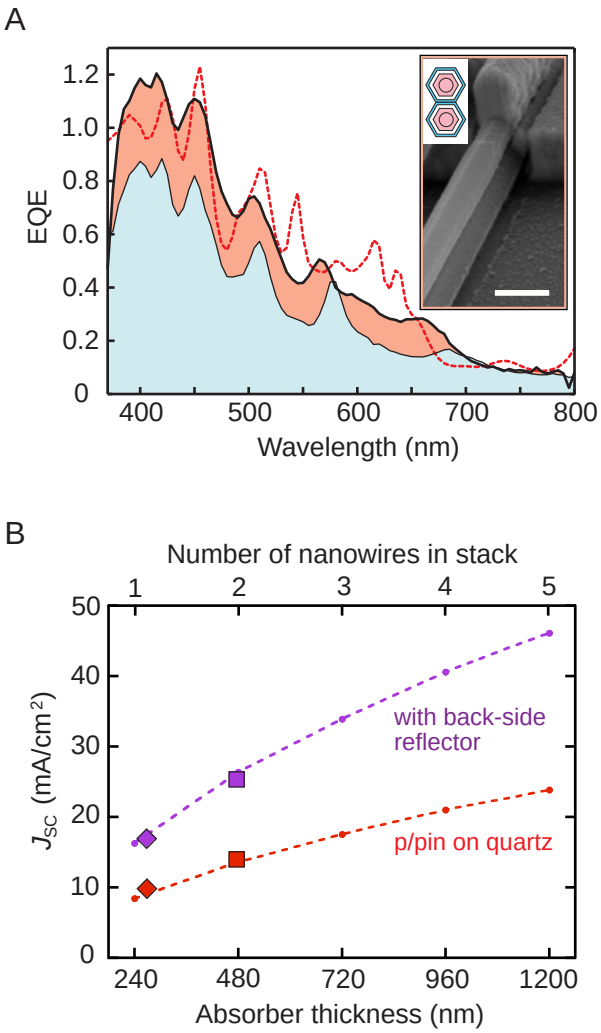
A
EQE
Wavelength (nm)
B
Number of nanowires in stack
J_{SC} (mA/cm^2)
Absorber thickness (nm)
with back-side reflector
p/pin on quartz

Figure 5

Supporting Information for:

Coaxial multishell nanowires with high-quality electronic interfaces and tunable optical cavities for ultrathin photovoltaics

Thomas J. Kempa, James F. Cahoon, Sun-Kyung Kim, Robert W. Day, David C. Bell, Hong-Gyu Park, and Charles M. Lieber

This PDF file includes:
Materials and Methods
Figures S1-S7 and Legends
Supporting References

Materials and Methods:

1. NW synthesis.

Au catalysts (100 nm diameter) were dispersed on poly-L-lysine functionalized 600 nm SiO_2-on-Si wafers. Substrates were inserted into a home-built reactor and the system evacuated to a base pressure of 2.8 mTorr. Crystalline p-type cores were grown at 470˚C and 40 Torr for 2.5 hours with flow rates of 1, 10, and 60 standard cubic centimeters per minute (sccm) for silane (SiH_4), diborane (B_2H_6, 100 p.p.m. in H_2), and hydrogen (H_2, Semiconductor Grade), respectively. All shell growth over these cores was performed at 775˚C and 25 Torr. Boron-doped p-type shells were grown for 25-30 min with 0.15, 1.5, and 60 sccm silane, diborane, and hydrogen, respectively. Intrinsic shells were grown for 20-25 min with 0.15, and 60 sccm silane and hydrogen, respectively. Phosphorous-doped n-type shells were grown for 10-15 min with 0.15, 0.75, and 60 sccm silane, phosphine (PH_3, 1000 p.p.m. in H_2), and hydrogen, respectively. The calibrated shell growth rates determined from independent studies of single shell thickness vs. growth time were 1.7, 1.7 and 3 nm/min for p, i and n, respectively. Following NW growth, a 30-40 nm conformal layer of SiO_2 was deposited using plasma enhanced chemical vapor deposition (PECVD) over the as-grown core/shell NWs.

2. NW shell synthesis on Au-catalyst-free NW cores.

Crystalline p-type NW cores were grown using the same core growth protocol as above. To remove the Au-catalyst following this low-temperature NW growth and prior to higher temperature shell growth, the NW cores were removed from the reactor and immersed in KI/I_2 solution for 2 min, rinsed in deionized water, then etched in buffered hydrofluoric acid (BHF) for 1 min, and rinsed once more in deionized water. Scanning electron microscopy (SEM) analysis of NWs etched by KI/I_2 demonstrated that the Au-catalyst was removed from the NW ends as reported previously for Ge NWs (S1). Following the last water rinse, the NW growth substrate was immersed in liquid N_2 and then placed under vacuum to remove residual water without aggregation of NWs by capillary action. Intrinsic, n-type and SiO_2 shells were then grown as described above.

3. Al-catalyzed NW synthesis.

A 10 nm thick Al film was deposited by thermal evaporation ($< 1.0 \times 10^{-7}$ Torr) onto a n-type <111> Si growth substrate, the substrate was inserted into the reactor, and the system was evacuated to a base pressure of 2.8 mTorr. The substrate was annealed for 1 min at 540˚C, the temperature was reduced to 510˚C, and 3 sccm of disilane (Si_2H_6) and 97 sccm of hydrogen were introduced with a total reactor pressure of 100 Torr. After 1 min, the temperature was reduced to 475˚C and growth proceeded for 15 min. Following NW core growth, the substrate was removed from the reactor, etched for 1 min in Al etchant (Transene) at 40˚C, etched 2 min in BHF, and then dried as described above for Au-etched NWs. The NW cores were annealed for 20 min

under vacuum at 775˚C and then p-type, intrinsic, n-type and SiO_2 shells were grown as described above.

4. TEM and EDS sample preparation and characterization.

Ultra-thin NW cross-sections for TEM investigations were prepared by embedding as-grown core/shell NWs in epoxy (Epo-Tek 353ND, Epoxy Technology) followed by degassing to remove air bubbles and overnight curing at 30˚C in a vacuum oven. ~40-60 nm thick samples were sectioned (Ultra Microtome, Leica) from the cured epoxy slugs using a diamond knife (Ultra 35˚, DiATOME) and transferred to lacey carbon grids for aberration corrected TEM analysis (cs-TEM, Libra 200-80 MC, Carl Zeiss NTS). For phosphorous dopant mapping by EDS, p/pin NWs were synthesized as described above with elevated phophorous doping in the n-shell (0.15, 7.5, and 60 sccm flow rates for silane, phosphine, and hydrogen, respectively). This strategy was necessary to increase signal-to-noise and to study the degree of dopant localization but not absolute concentration (~$1x10^{20}$ cm^{-3}). The aberration corrected scanning TEM (cs-STEM, Libra 200 MC, Carl Zeiss NTS) used for acquisition of EDS elemental maps is equipped with twin EDS detectors and drift correction. The EDS spectra and EDS elemental map for P are shown in Fig. S2. Maps were stored at 1024x800 resolution and acquired over 5 hours using a 400 ms pixel dwell time and 1.2 nm spot size. The P and O profiles plotted in Fig. 1E were obtained by averaging 200 line scans across the P and O EDS maps associated with the boxed region of the inset STEM image. The P and O line profiles also reflect a running average of +/– 10 points.

5. NW device fabrication.

NWs were shear transferred from growth substrates to Si_3N_4 or quartz device chips (S2). 500 nm of SU-8 2000.5 was spin-coated on the device substrate, pre-baked (95˚C), and photolithography or electron beam lithography (EBL) was performed to define SU-8 etch masks on the NW shells. The SU-8 was subsequently developed and cured at 180˚C for 10 min. Following a 20 s BHF etch to remove the SiO_2 outer shell, the NWs were etched for 10–18 s in potassium hydroxide (KOH 38 vol.% in water) at 60˚C. Last, EBL followed by thermal evaporation of 4 nm of Ti and 350 nm of Pd yielded selective patterned contacts to the etched (p-type) core and un-etched (n-type) shell. A 10 nm film of Ni, which serves as a charge dissipation layer, was deposited over resists for EBL fabrication on quartz substrates.

6. Device measurements.

A standard solar simulator (150W, Newport Oriel) with AM 1.5G filter and calibrated 1-sun intensity was used in conjunction with a probe station (TTP-4, Desert Cryogenics) and semiconductor parameter analyzer (4156C, Agilent Technologies) to obtain all device transport characteristics. Wavelength dependent photocurrent spectra were obtained with a home-built optical setup utilizing the solar simulator with AM 1.5G filter as illumination source and a spectrometer (SpectraPro 300i, Acton Research) with 1200 g/mm grating and blaze angle of 500

nm. An uncoated Glan-Thompson calcite polarizer (10GT04, Newport) and power meter with low power Si photodetector (1918-C and 918D-UV-OD3, Newport) were used to obtain polarization-resolved absolute external quantum efficiency (EQE) spectra. The illumination power was measured from 300 to 900 nm in 5 nm increments through 1.0, 1.3, and 2.0 mm diameter circular apertures to confirm uniformity and accuracy of the power density used to calculate absolute EQE values. Device photocurrents for TE and TM polarizations were measured from 300 to 900 nm in 5 nm increments using a semiconductor parameter analyzer (4156C, Agilent Technologies). Unpolarized EQE spectra (Fig. 3) were calculated by averaging EQE data from TE and TM polarization measurements. Note that direct measurement of unpolarized spectra is not possible because of polarizing effects due to the grating and other optics used for measurement. However, the average of TE and TM spectra is equivalent to an unpolarized spectrum, because unpolarized illumination is composed of two equal, orthogonal polarization states represented by TE and TM polarizations (S3). Current density and absolute EQE were calculated using photocurrent data collected as described above and the projected area of the Si NWs, which was measured by SEM (Zeiss Ultra55). In our analyses, the projected area of a NW device was taken to be the entire exposed area of the unetched NW shell when viewed normal to the plane of the substrate and does not include the area covered by 350 nm thick Ti/Pd contacts. We note that this yields an upper limit to the J_{SC} that could be achieved in a practical device.

7. FDTD calculations.

For a normally incident plane wave with transverse electric (TE) and transverse magnetic (TM) orthogonal states, the absorption cross section of a NW or bulk Si was obtained by integrating $J \cdot E$ at each grid point, where J and E are the polarization current density and electric field, respectively. For NWs (bulk Si), the absorption cross section (absorption efficiency) was integrated over one optical period, and the wavelength of the normally incident plane wave was scanned from 280 – 1000 nm with a step size of 5 nm. For NWs, the absorption efficiency was defined by the ratio of the NW absorption cross section to the physical cross section. EQE was calculated by multiplying the absorption efficiency by internal quantum efficiency (IQE), where IQE was assumed to be unity. The short circuit current density (J_{SC}) at a specific wavelength was calculated as follows: $J_{SC}(\lambda)$ = EQE x (spectral irradiance of AM1.5 G spectrum at 1-sun solar intensity) x $\lambda/1.24$. The total J_{SC} was obtained by integrating $J_{SC}(\lambda)$ over the wavelength range of 280 – 1000 nm. For bulk Si simulations, a spatial resolution of 5 nm was used for the x, y and z directions and periodic boundary conditions were applied along the x and y directions. A perfectly matched layer was in contact with the lower z boundary of Si. For NWs, a spatial resolution of $5/\sqrt{3}$, 5, and 5 nm for x, y and z, respectively, was used to represent the volume element for our hexagonal cross section of a NW, where y lies along the NW axis and z lies along the propagation direction of the incident plane wave. All NW simulations included the substrates and conformal SiO_2 layer used in the experiment. Periodic boundary conditions were applied along the axis of a NW. Perfectly matched layers were applied at the other boundaries of the calculation domain. The total-field scattered-field (TFSF) method was applied to ensure that a single NW experiences an infinite plane wave. Without this method, the single NW would be simulated as a periodic array of NWs along the x-axis. To model the dispersive properties of the Si NW and Ag as a back-side reflector, the Drude-critical points model was incorporated into the

FDTD calculation (S4). The plasma and collision frequencies were obtained by fitting the measured refractive index and extinction coefficient of single crystal silicon (S5) and silver (S6) over the wavelength range, 280 – 1000 nm.

8. NW assembly.

First, shear transfer (S2) was used to assemble the first level of NWs (the bottom NW in a vertical stack) onto quartz device substrates. After spin coating poly(methyl methacrylate) (PMMA) C5 over the device substrate, electron beam lithography was performed to open 0.5 μm wide trenches over selected NWs. A second layer of NWs was transferred over the patterned PMMA, followed by addition of a water droplet, which was blown across the device region using dry N_2. After this process, NWs were drawn into the trenches defined over the first level NWs to yield two vertically stacked NWs. PMMA was removed with a UV/O_3 asher at 200˚C for 10 min, and subsequent device fabrication proceeded as described above.

9. Dark saturation current. Dark current-voltage (*I*-V) measurements for each NW were fit within the linear regime to extract I_0 from the ideal diode equation, $\ln(I)=qV/(nkT)+\ln(I_0)$, where q is elementary charge, V is voltage, n is the diode ideality factor, k is the Boltzmann constant, and T is temperature.

10. Comparison of V_{OC} between planar and NW devices.

We have also compared our coaxial Si NW device characteristics to those of planar Si solar cells as a means to measure their performance and potential for improvement. The direct comparison of V_{OC} discussed in the main text shows a lower value for our NW devices. We wish to assess whether higher V_{OC}'s could be obtained through further improvement of, for example, junction quality in these NW structures. Before addressing this question, we estimated the contributions to lower V_{OC} in coaxial NWs arising from differences in their geometry and their incomplete light absorption relative to planar Si solar cells.

First, and as discussed previously (S7, S8), there is a larger p-n or p-i-n junction area for devices with cylindrical versus planar geometries for a given projected area. The change in V_{OC} due to increased junction area of a cylindrical structure can be accounted for by a logarithmic dependence on γ, which relates the junction area in a NW to the junction area in a planar device with an equivalent projected area as reported (S7, S8):

$$V_{OC} = (nk_BT/q)\, ln\, (I_{SC}/\gamma I_0), \qquad \text{(Eq 1)}$$

where n is the ideality factor, k_B is the Boltzmann constant, q is charge, I_{SC} is the short-circuit current, and I_0 is the dark saturation current. We estimate γ by assuming the NWs are perfect cylinders with a junction area defined by the outside surface of the cylinder, yielding $\gamma = \pi$. Using the parameters for one of the better p/in devices (V_{OC} = 0.475 V; n = 1.61; I_{SC} = 155 pA; I_0 = 1.1 fA), we calculate a positive shift in V_{OC} of ΔV_{OC} = 0.044 V and a final V_{OC} of 0.519 V.

Second, we can also account for the effect of incomplete light absorption in the coaxial Si NW devices by introducing a factor α, which relates the I_{SC} of a NW device to that of a conventional Si solar cell with complete light absorption as:

$$V_{OC} = (nk_BT/q)\ ln\ (\alpha I_{SC}/\gamma I_0), \qquad \text{(Eq 2)}$$

We estimate α by noting that the short-circuit current density (J_{SC}) of our p/in NWs is 6-7 mA/cm^2 whereas the J_{SC} of state-of-the-art bulk Si solar cells (S9) is ~43 mA/cm^2. Using a value of $\alpha = 7$ and $\gamma = \pi$, we arrive at $\Delta V_{OC} = 0.119$ V and a final V_{OC} of 0.594 V. The values of V_{OC} for high-quality multicrystalline and single crystal Si solar cells with complete light absorption are 0.66 – 0.7 V (S9). Hence, we can conclude that our measured coaxial NW V_{OC} is close to the best that might be expected (with the above corrections), although the difference of 0.07 to 0.11 V does suggest that further improvement might be achieved by additional optimization of the core/shell structures and surface passivation.

Supplementary Figure Legends:

Fig. S1. SEM images of as-grown core/shell Si NWs. *(A)* p/n NW showing a smooth, faceted surface for the majority of the NW but some surface roughness toward the tip of the NW. Markings and lettering result from measurement of the NW diameter, which is ~265 nm; scale bar, 200 nm. *(B)* p/pn NW showing a smooth surface and faceted tip. Markings and lettering result from measurement of the NW diameter, which is ~300 nm; scale bar, 200 nm. *(C)* p/pin NW showing a smooth, faceted surface and faceted tip. NW diameter is ~360 nm; scale bar, 200 nm.

Fig. S2. EDS spectra of p/pin NW sections for P dopant profiling. *(A)* EDS spectrum from 0 – 2.2 keV after 5 hour acquisition from an ~60 nm thick p/pin NW section. Peaks characteristic of specific elements are labeled and are identified in the panel at right. *(B)* EDS spectra from 1.6 – 2.2 keV corresponding to inner-shell (blue) and outer-shell (black) regions of the NW cross section. Right-hand panel shows a spatial map of P X-ray counts (red), which appear in greater number and density within the outer 20-30 nm of the cross section. Inset displays the STEM image of the cross section; scale bar 100 nm. The inner-shell (blue) and outer-shell (black) spectra represent a sum of all X-ray counts within the two blue and two black boxed regions, respectively. The spectra demonstrate that X-ray counts from the outer-shell region give rise to a peak clearly identifiable as P and distinguishable from the background. X-ray counts from the inner region do not produce a clear P peak and are attributed to a combination of dark counts and the tail of the strong Si peak. The line profile for P in Fig. 1E was calculated from the same data set, where the large apparent background signal for the central ~300 nm of the P line profile in Fig. 1E is also attributable to a combination of dark counts and the tail of the strong Si peak.

Fig. S3. Measured light *I*-V characteristics for different NW structures. Illuminated current-voltage (*I*-V) traces for the 4 NW devices shown in Fig. 2B. Results show that all devices routinely exhibit I_{SC} values greater than 100 pA and that transport characteristics are recorded at high resolution to enable precise measurement of device metrics (I_{SC}, V_{OC}, FF).

Fig. S4. Synthesis and fabrication of Al-catalyzed i/pin NW devices. *(A)* SEM image of Al-catalyzed intrinsic Si NW cores that are 30-50 μm long, 70-120 nm in diameter, and exhibit ~25 nm of radial taper over 30 μm; scale bar, 20 μm. *(B)* SEM images of coaxial NWs after growth of p-i-n shells on the Al-catalyzed cores. The NW surface is relatively smooth over the length of the NW (left panel; scale bar, 2 μm) but is not as smooth and faceted as observed for Au-catalyzed core/shell NWs. Faceted surfaces were typically found within 10 μm of the NW tip (right panel; scale bar, 200 nm). *(C)* SEM image of an Al-catalyzed i/pin NW solar cell (*I*-V data for this device are plotted as the grey curve in Fig. 2D); scale bar, 1 μm. Comparison of the V_{OC} (I_0) metrics for Al- and Au-catalyzed i/pin NW devices, 0.23 V (0.8 pA) and 0.40 V (13.0 fA), respectively, highlights the substantially-improved electrical quality of NWs synthesized from Au-catalyzed cores. Devices were fabricated using the same protocol as for other NWs (see Methods).

Fig. S5. Scaling of photocurrent with NW length. I_{SC} (red squares) and J_{SC} (blue squares) values for 14 p/pin devices plotted as functions of the exposed NW length. Results show that I_{SC} scales linearly over a range of NW lengths spanning at least one order of magnitude with values ranging from 114 pA (4.3 μm) to 1186 pA (47.3 μm). The corresponding J_{SC} values for these devices, 9.9 and 8.4 mA/cm^2, and average for all of the 14 devices, 10.0 +/- 0.7 mA/cm^2 show that J_{SC} is relatively constant as expected.

Fig. S6. External quantum efficiencies for p/in and p/pin NWs at TE and TM polarizations. *(A)* Schematic of the transverse-electric (TE) and transverse-magnetic (TM) electric field polarizations relative to the NW structure. *(B and C)* External quantum efficiency (EQE) as a function of wavelength (black curves) measured for a p/in NW *(B)* and p/pin NW *(C)* using TE (top) and TM (bottom) polarizations. Red dashed curves are FDTD simulations (see Methods) assuming a hexagonal shape for the NW and height of 240 nm for the p/in and 305 nm for the p/pin NW. The mode spatial profiles of peaks labeled 1 – 6 in the TM spectra are illustrated in Fig. 3C and are labeled identically in the manuscript. Peaks in the spectra correspond to absorption in the NW due to either Fabry-Perot or whispering-gallery resonant modes. These modes shift in frequency as the diameter of the NW varies. Specifically, many of the differences between the spectra of the p/in and p/pin NW can be explained by the ~80 nm larger diameter of the latter. In addition, the p/pin structure supports a larger number of resonant modes, thus explaining the large number of peaks present in the p/pin spectrum versus the p/in spectrum.

Fig. S7. NW vertical stacks. *(A)* Simulated absorption mode profiles of the double-NW stack for TE polarization at λ=425 nm (left) and for TM polarization at λ=545 nm (right). The absorption modes present in the top NW are preserved in the bottom NW, and this effect permits the broadband enhancement observed in the experimental and simulated EQE spectra for the double-NW stack (Fig. 4B). *(B)* Simulated EQE spectra for a 5-NW vertical stack (red curve) and a single micron-wire (black) with equivalent Si height to the 5-NW stack. Inset: schematic comparing a 5-NW vertical stack against a single micron-wire with Si height (1200 nm) equivalent to that of the stack. The 5-NW stack attains a maximum EQE of 1.74, which is substantially larger than the maximum of 0.97 for the single micron-wire of equal height. The EQE > 1 is a manifestation of the fact that individual NWs within the stack exhibit absorption cross-sections greater than their physical cross-sections and thus absorb photons from outside of their physical projected area; this is referred to as the optical antenna effect (S10).

Supplementary References:

S1. Woodruff JH, Ratchford JB, Goldthorpe IA, McIntyre PC, Chidsey CED (2007) Vertically oriented germanium nanowires grown from gold colloids on silicon substrates and subsequent gold removal. *Nano Lett.* 7:1637-1642.

S2. Javey A, Nam SW, Friedman RS, Yan H, Lieber CM (2007) Layer-by-layer assembly of nanowires for three-dimensional, multifunctional electronics. *Nano Lett.* 7:773-777.

S3. Hecht E (2002) *Optics* (Addison Wesley, San Francisco).

S4. Vial A, Laroche T (2008) Comparison of gold and silver dispersion laws suitable for FDTD simulations. *Appl. Phys. B: Lasers Opt.* 93:139-143.

S5. Lide DR (2008) *CRC handbook of chemistry and physics: a ready-reference book of chemical and physical data* (CRC Press, Boca Raton).

S6. Johnson PB, Christy RW (1972) Optical constants of the noble metals. *Phys. Rev. B* 6:4370-4379.

S7. Kayes BM, Atwater HA, Lewis NS (2005) Comparison of the device physics principles of planar and radial p-n junction nanorod solar cells. *J. Appl. Phys.* 97:114302-114311.

S8. Boettcher SW *et al.* (2010) Energy conversion properties of vapor-liquid-solid-grown silicon wire-array photocathodes. *Science* 327:185-187.

S9. Green MA, Emery K, Hishikawa Y, Warta W (2010) Solar cell efficiency tables (version 36). *Prog. Photovoltaics* 18:346-352.

S10. Cao LY *et al.* (2010) Semiconductor nanowire optical antenna solar absorbers. *Nano Lett.* 10:439-445.

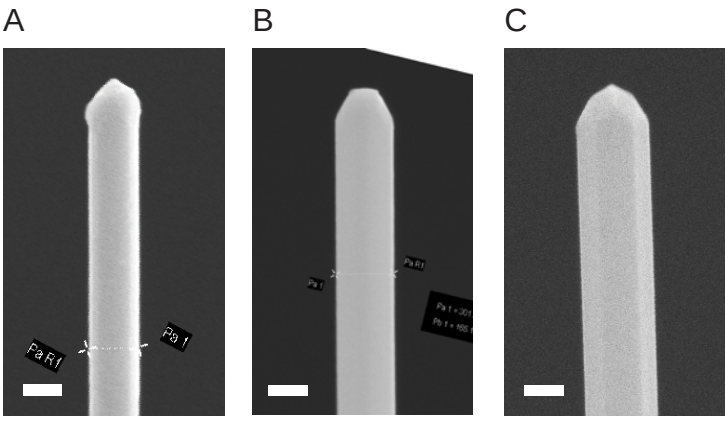

Supplementary Figure S1

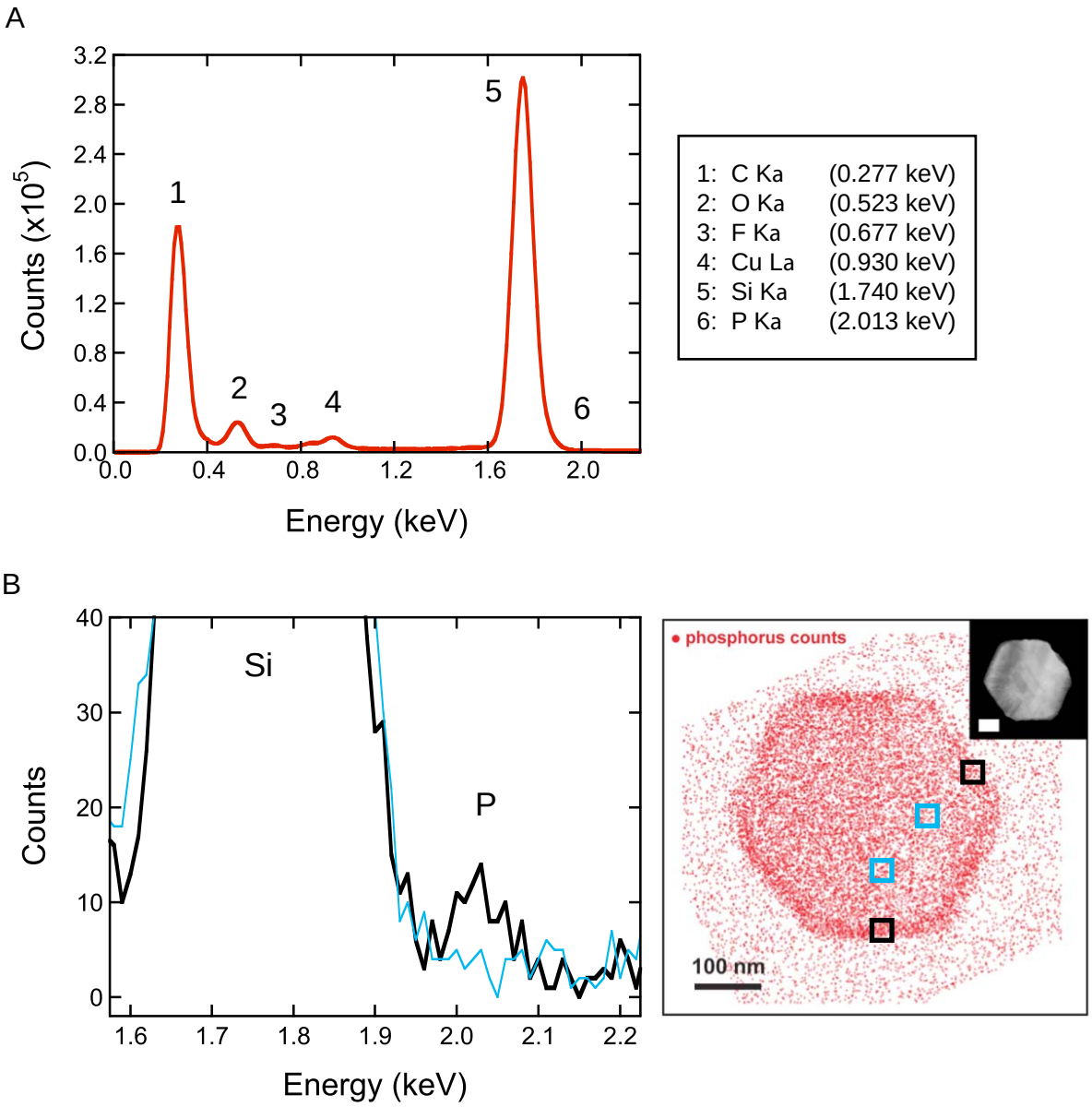

Supplementary Figure S2

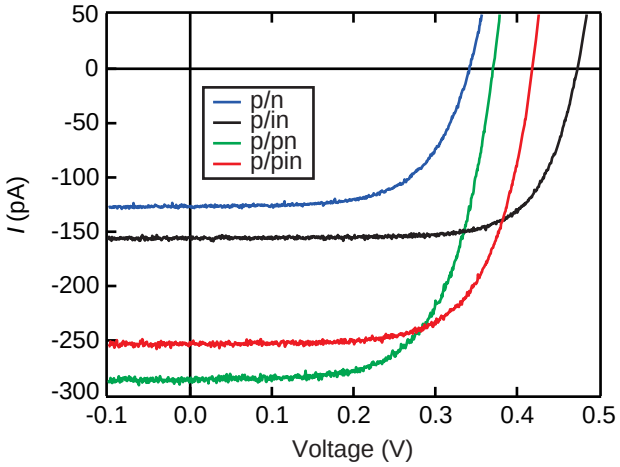

Supplementary Figure S3

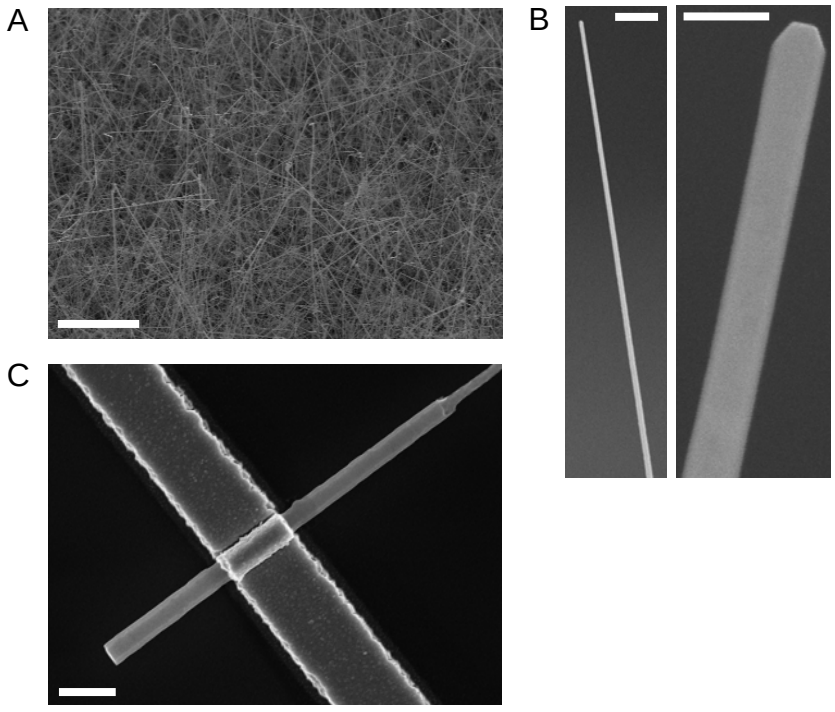

Supplementary Figure S4

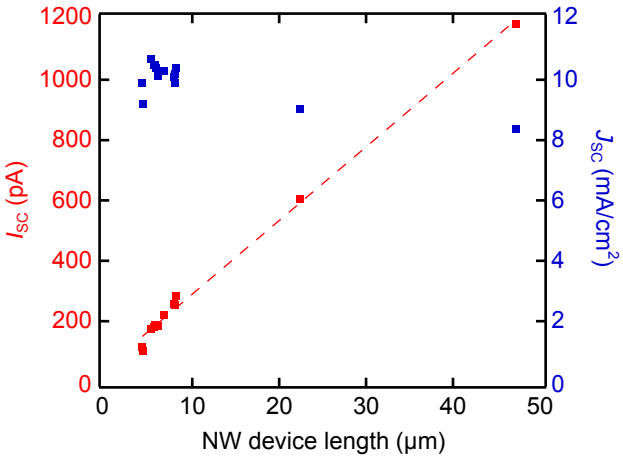

Supplementary Figure S5

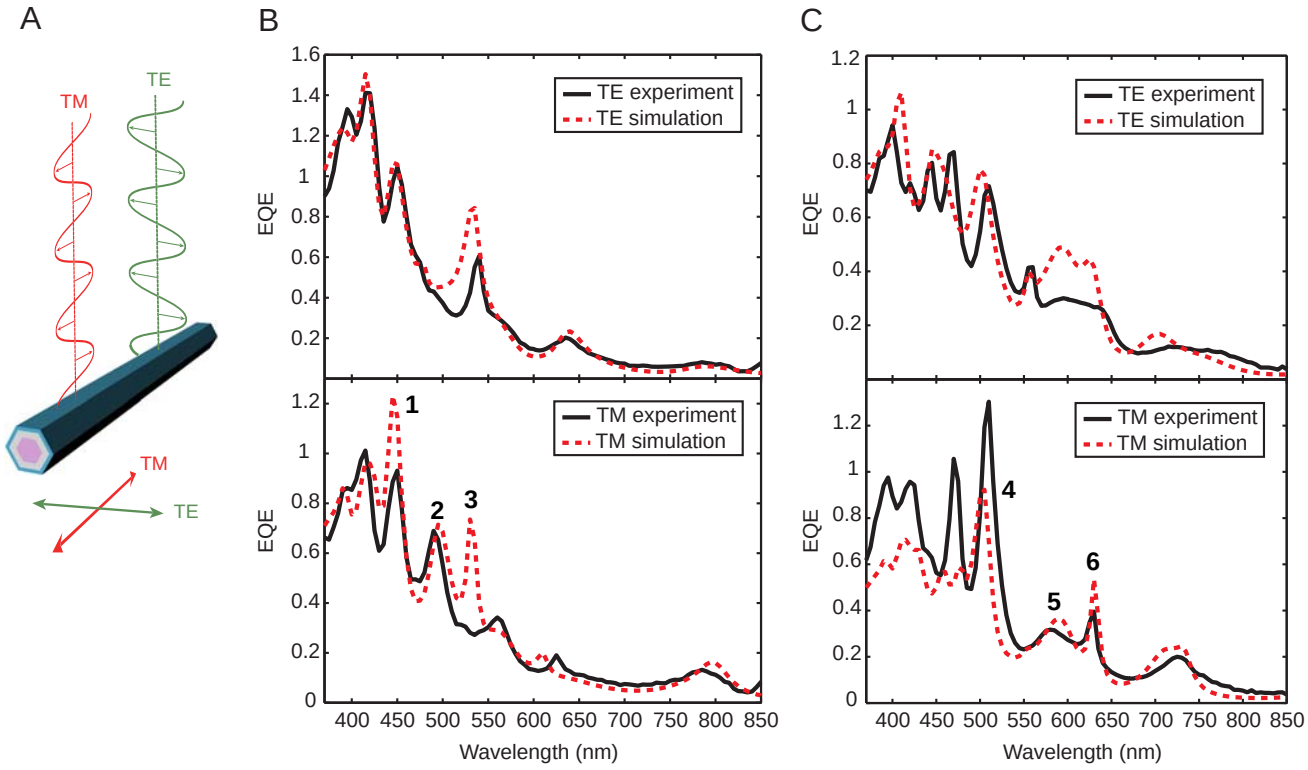

Supplementary Figure S6

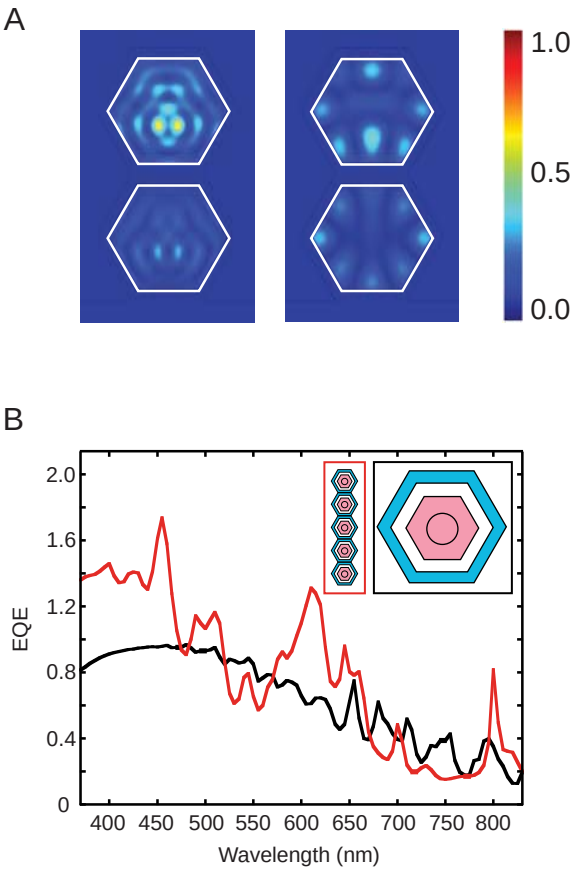

Supplementary Figure S7